RESEARCH ARTICLE

Key Points:
- This study shows that refractive index correlates with bulk and glass major oxide compositions of volcanic ash over a broad spectral range
- A parameterization of complex refractive index is developed based on the silica content and NBO/T of volcanic ash using the correlation found
- Mass loading retrievals using the parameterization show significant differences compared to those using a generic complex refractive index

Supporting Information:
- Supporting Information S1
- Figure S1
- Figure S2
- Figure S3
- Figure S4
- Data Set S1
- Data Set S2

Correspondence to:
G. S. Prata,
gemma@aires.space

A New Parameterization of Volcanic Ash Complex Refractive Index Based on NBO/T and SiO$_2$ Content

G. S. Prata[1] [iD], L. J. Ventress[2], E. Carboni[3] [iD], T. A. Mather[1] [iD], R. G. Grainger[2], and D. M. Pyle[1] [iD]

[1]COMET, Department of Earth Sciences, University of Oxford, Oxford, UK, [2]National Centre for Earth Observation (NCEO), Atmospheric, Oceanic and Planetary Physics, University of Oxford, Oxford, UK, [3]COMET, Atmospheric, Oceanic and Planetary Physics, University of Oxford, Oxford, UK

Abstract Radiative transfer models used in remote sensing and hazard assessment of volcanic ash require knowledge of ash optical parameters. Here we characterize the bulk and glass compositions of a representative suite of volcanic ash samples with known complex refractive indices ($n + ik$, where n is the real part and k is the imaginary part). Using a linear regression model, we develop a new parameterization allowing the complex refractive index of volcanic ash to be estimated from ash SiO$_2$ content or ratio of nonbridging oxygens to tetrahedrally coordinated cations (NBO/T). At visible wavelengths, n correlates better with bulk than with glass composition (both SiO$_2$ and NBO/T), and k correlates better with SiO$_2$ content than with NBO/T. Over a broader spectral range (0.4–19 μm), bulk correlates better than glass composition, and NBO/T generally correlates better than SiO$_2$ content for both parts of the refractive index. In order to understand the impacts of our new parameterization on satellite retrievals, we compared Infrared Atmospheric Sounding Interferometer satellite (wavelengths 3.62–15.5 μm) mass loading retrievals using our new approach with retrievals that assumed a generic (Eyjafjallajökull) ash refractive index. There are significant differences in mass loading using our calculated indices specific to ash type rather than a generic index. Where mass loadings increase, there is often improvement in retrieval quality (corresponding to cost function decrease). This new parameterization of refractive index variation with ash composition will help to improve remote-sensing retrievals for the rapid identification of ash and quantitative analysis of mass loadings from satellite data on operational timescales.

1. Introduction

Satellite retrievals of volcanic ash clouds are important for hazard assessment and the understanding of volcanic processes. At present, there are limited data available on the optical properties of different ash types and no systematic way of predicting optical properties for unknown samples. Fine volcanic ash (<63-μm diameter) makes up between a few percent to over 50% of the mass proportion in explosive eruptions (Rose & Durant, 2009) and is typically composed of a mixture of silicate glass particles and crystals. The atmospheric residence time of fine ash, depending on its grain size and atmospheric conditions, may range from hours to weeks or months (Cashman & Rust, 2016). Satellite observations from eruptions in the Southern Hemisphere (Barton et al., 1992; Klüser et al., 2013) have demonstrated that ash plumes can be transported for 1,000 km downwind. Long residence times and long-range transport of volcanic ash may have significant implications for aviation far from the volcanic source (Casadevall, 1994; Prata & Tupper, 2009), and for this reason it is important to be able to reliably retrieve ash mass loading from remote sensing data. In order to detect and quantify the properties of an ash plume using satellite remote sensing, knowledge of the optical properties of volcanic ash is necessary. These optical properties are governed by the complex refractive index ($n + ik$). Both real (n) and imaginary (k) components are required to retrieve quantitative estimates of mass loading from satellite images and hence concentrations (if the cloud thickness is known or assumed). The top of atmosphere radiation, measured by imaging and sounding instruments on board satellites, is also dependent on the particle-size distribution and the shape of the particles (Clarisse & Prata, 2016).

The refractive index of volcanic glass is principally controlled by its composition; a feature that has previously been utilized as a rapid way to characterize volcanic ash type (e.g., Keller et al., 1978). Pollack et al. (1973) reported complex refractive indices in the spectral range 0.21–50 μm using a combination of transmission and reflectivity measurements on polished rock slabs ranging in composition from

basalt to obsidian (53.25–76.2 wt.% SiO_2). In the same year, Volz (1973) reported the complex refractive index for volcanic pumice in the spectral range of 2.5–40 μm. Previous studies of ash cloud properties using satellite retrievals from the eruption of Mt. Spurr, Alaska, in 1992 (Wen & Rose, 1994) and the eruption of Mt. Ruapehu, New Zealand, in 1996 (Prata & Grant, 2001) found the "andesite" refractive index of Pollack et al. (1973) to be the most suitable approximation. Most volcanic ash retrieval schemes use refractive index data from either the Pollack et al. (1973) or Volz (1973) data sets (Francis et al., 2012); however, as these are from measurements of rock slabs or pumice, neither of these are representative of natural ash particulate samples.

The challenge in measuring complex refractive indices based on transmission or reflectance spectra comes from the difficulty in estimating n, which influences scattering. Planar surfaces do not scatter as much as particles of the same material due to the presence of multiple-scattering surfaces. Therefore, spectral reflectance measurements on polished slabs, such as those of Pollack et al. (1973), may significantly underestimate the influence of scattering by not accounting for directionality and so underestimate the contribution of n. For this reason, measurements on dispersed particles are preferred, but this also requires accurate knowledge of the particle-size distribution. Recently, new methods have been proposed that combine particle-size distribution measurements to retrieve aerosol complex refractive indices from high-resolution extinction spectra (Herbin et al., 2017; Reed et al., 2017).

Previous refractive index measurements of volcanic ash have been made on samples from Mt. Mayon in the range of 1–16 μm (Patterson, 1975), Mt. St. Helens and El Chichón in the range of 0.3–0.7 μm (Patterson, 1981; Patterson et al., 1983), and Eyjafjallajökull in the range of 0.3–2.5 μm (Rocha-Lima et al., 2014). However, these only included the imaginary part of the complex refractive index. Measurements of both parts (n and k) have been made in the range of 0.3–0.4 μm for Mt. Spurr ash (Krotkov et al., 1999). Recently, Vogel et al. (2017) provided a new comprehensive data set of volcanic ash optical and physicochemical properties in the range of 0.3–1.5 μm. This data set includes a broad range of compositions and provides a useful reference for complex refractive indices in the ultraviolet to near-infrared range but does not include longer wavelengths (midinfrared range), which are necessary for deriving mass loadings from the silicate absorption feature between 8 and 12 μm (Clarisse & Prata, 2016). Complex refractive indices for the samples used in the present study have been presented in Grainger et al. (2013), Ball et al. (2015), and Reed et al. (2018) over a wide spectral range (0.33–20 μm). One of the main challenges in selecting an appropriate refractive index in the event of an eruption is that the volcanic ash composition is typically not known until afterward and composition of the cloud becomes more silicic downwind, as denser crystals settle more rapidly than the glassy components (Cashman & Rust, 2016). With the exception of the new Vogel et al. (2017) data set, to date, there are few systematic data that show how volcanic ash optical properties relate to composition The lack of a parameterization of this kind is an important source of uncertainty in retrieval schemes (Francis et al., 2012; Mackie et al., 2014).

The spectral signature of silicates in the visible range is dominated by scattering, with only a small component of absorption; silica glass is typically transparent in this range (Kitamura et al., 2007). In the infrared, silicate absorption is dominated by a peak between 8 and 12 μm associated with resonances of the stretching vibration of the $T–O^-$ bond (Clarisse & Prata, 2016; Clark, 1999; Kieffer, 1979; Kitamura et al., 2007), where T is a tetrahedrally coordinated cation. The length of this bond determines the frequency at which radiation is absorbed, with longer bonds corresponding to lower frequencies (Kieffer, 1979; Walter & Salisbury, 1989). Bond length within the tetrahedral framework in silicate glass is influenced by the extent to which tetrahedral Si cations are substituted with other network formers (Fe^{3+}, Al^{3+}, Mg^{2+}, and P^{5+}) and by the addition of other divalent cations (Fe^{2+}, Ca^{2+}, and Mg^{2+}) that act as network modifiers breaking up the tetrahedral network (Mysen & Richet, 2005). Depolymerization of the structure results in bond lengthening, so the material absorbs radiation at progressively lower frequencies as its vibrational frequencies decrease, resulting in a shift of the $T–O^-$ bond absorption feature toward longer wavelengths. Breaking up the tetrahedral network also results in the generation of nonbridging oxygens (NBO). The ratio of nonbridging oxygens to tetrahedrally coordinated cations (NBO/T) can be calculated from oxide weight percentages (Mysen et al., 1982). NBO/T has been shown to be a good measure of depolymerization (Di Genova et al., 2015; Mills, 1993), making it a useful parameter to investigate the relationship between composition and optical properties.

Table 1
Description of Volcanic Ash Samples

Volcano	Eruption unit/date where known	Refractive index data set
Askja[a]	Layer C 1875	1, 2
Aso	1993	1, 2
Augustine[b]	June 2006	1
Chaitén[c]	May 2008	1
Etna	1 November 2002	1
Eyjafjallajökull (a)	19–20 May 2010	2
Eyjafjallajökull (b)	15–16 May 2010	1, 2
Grimsvötn (a)	May 2011	2
Grimsvötn (b)	May 2011	1
Nisyros[d]	? > 44 Ka BP	1, 2
Okmok[e]	12 July 2008	1
Spurr[f]	August 1992	1, 2
Tongariro	2012	1, 2

Note. Samples used in Ball et al. (2015) are labeled as Data Set S1, and those used in Reed et al. (2018) are labeled as Data Set S2. References where samples have previously been described are included.
[a]Sparks et al. (1981). [b]Larsen et al. (2010). [c]Watt et al. (2009). [d]Longchamp et al. (2011). [e]Larsen et al. (2013). [f]Harbin et al. (1995).

NBO/T has potential advantages over simply using SiO_2 content, which we will test in this study, as it allows further discrimination of absorption features between different silicate compositions. The dependence of the $T–O^-$ bond absorption feature on the degree of silicate polymerization has previously been used in remote-sensing applications for determining rock composition in the infrared (e.g., Walter & Salisbury, 1989) and more recently in estimating composition using Raman spectroscopy (e.g., Di Genova et al., 2015). While silicate infrared absorption is the basis for the remote sensing of volcanic ash clouds, the ability to determine ash composition from infrared spectra is only beginning to be explored (Clarisse et al., 2010; Gangale et al., 2010).

In this study we characterize the compositions of a suite of volcanic ash samples and explore the relationship between composition (SiO_2 and NBO/T) and the complex refractive index measurements of the same samples reported in Ball et al. (2015) and Reed et al. (2018). We have used the Reed et al. (2018) data set to develop an empirically based parameterization of complex refractive index. Finally, we investigate the recent eruptions of Grímsvötn, Iceland (May 2011); Chaitén, Chile (May 2008); and Okmok, Aleutian Peninsula (July 2008), in order to assess the usefulness of our parameterization in infrared satellite ash retrieval schemes.

2. Methods

2.1. Compositional Analysis

Samples of dry-sieved volcanic ash (<100 μm), with complex refractive index data available (Ball et al., 2015; Reed et al., 2018), were selected from a broad compositional range of eruptions (Table 1). Major elements of the bulk ash were determined by X-ray fluorescence (XRF) on fused glass beads prepared from ignited powders of the <100-μm fraction with a sample to flux ratio of 1:5, 80% Li metaborate:20% Li tetraborate flux. Analyses were carried out on a PANalytical Axios-Advanced XRF spectrometer at the Department of Geology, University of Leicester. Components with concentrations below the lower limit of detection are reported as <LLD. The detection limits vary according to each element, and counting statistical errors vary by sample. These errors are typically <0.004%, so they do not significantly impact further calculations.

Subsamples were taken in order to measure the major elements of the glass components. These were analyzed using a Jeol JXA8600 electron probe microanalyzer (EPMA) with wavelength dispersive spectroscopy at the Research Laboratory for Archaeology and the History of Art, University of Oxford. Compositions were obtained by averaging analyses of glass shards (20–100 μm) with a spot size of 10-μm diameter, accelerating voltage of 15 kV, and 6-nA beam current and calibrated using a suite of mineral standards (Jochum et al., 2006).

The calculation of NBO is based on electrical charge balance, that is, the difference between the total negative charge (O^{2-}) and the positive charge of tetrahedral (T) cations. For melts with several types of potential T cations, the calculation relies upon knowing the structural role of all cations. In order to do this, the chemical analysis of the sample is converted to atomic proportions. Cations Si^{4+}, Ti^{4+}, and P^{5+} are assigned to the role of T, and Al^{3+} and Fe^{3+} are assigned the role of T if there are excess alkalis available for charge balance. The ratio is then obtained by dividing NBO by the total of T cations according to Mysen and Richet (2005) and Giordano et al. (2008) using the equation from Mysen et al. (1982):

$$\frac{NBO}{T} = \frac{(2 \times O)(4 \times T)}{T}, \tag{1}$$

assuming that Si^{4+}, Ti^{4+}, P^{5+}, Al^{3+}, and Fe^{3+} are in charge-balanced tetrahedral coordination. See the spreadsheet provided in Data Set S1 in the supporting information for a detailed calculation of NBO/T. Proportions of Fe_2O_3 and FeO were estimated from total iron using ferric/ferrous iron ratios (f) suggested by Middlemost (1989) for each volcanic rock type as classified on the total alkalis versus silica diagram. This assumption is

based on the fact that the primary influence on Fe speciation is the oxidation state of the magma and does not take into account any in-plume processing that may alter the ferric/ferrous iron ratio of the ash (e.g., Ayris & Delmelle, 2012).

2.2. Refractive Index Measurements

The real and imaginary parts of the refractive index for these samples have been reported in Ball et al. (2015) and Reed et al. (2018). These studies used two different techniques in order to obtain the complex refractive index. Ball et al. (2015) used a direct method, the Becke Line method, to estimate the real part by immersing particles in oils of known refractive index. The particles suspended in oil are viewed through a transmitted light microscope through filters of a specific wavelength (450, 546.7, and 650 nm). The light refracted at the edge of the particle moves into or out of the material as the stage is brought into focus; this way the real part of the refractive index can be estimated in comparison to the oil in which it is suspended. Once the real part is known, the particles can be suspended in an oil of matching refractive index, and the imaginary part is estimated by measuring the intensity of the light passing through, as any attenuation will be due to absorption. See Ball et al. (2015) for a more detailed explanation. In contrast, Reed et al. (2018) used an indirect method to retrieve the complex refractive index by measuring the spectral extinction measurements over the range of 0.33–19 μm. This was done using a Fourier transform spectrometer, which covered the infrared wavelengths, and two diffraction grating spectrometers, covering the visible and ultraviolet wavelengths. The size distribution was measured concurrently using a scanning mobility particle sizer. Knowledge of the particle-size distribution allowed the complex refractive index of the particles to be obtained, once the H_2O and CO_2 gas absorption lines were removed from the extinction spectra. A detailed description of the retrieval method is given in Reed et al. (2017).

2.3. Parameterization

We investigated the relationship between the complex refractive index (*n* and *k*) and bulk and glass composition (SiO_2 and NBO/T) at wavelengths 450, 546.7, and 650 nm from Ball et al. (2015) and in the wavelength range 0.4–19 μm from Reed et al. (2018). See Table 1 for the list of samples belonging to each data set. It was not possible to separately determine the composition using XRF or EPMA of the submicron size fraction on which the refractive index measurements had been made, given the quantity of sample and size of particles required for such measurements. Therefore, we determined the goodness of fit to a linear regression model using both bulk ash and glass compositions and compared the two.

2.4. Infrared Atmospheric Sounding Interferometer Retrieval Test Cases

In order to test the parameterization, complex refractive indices (*n* and *k*) were calculated from the NBO/T of Grímsvötn, Chaitén, and Okmok from our compositional data set. The calculation was done by deriving coefficients from the linear regression parameterization at each wavelength to "reconstruct" a spectrum for *n* and *k*. This calculation is provided in section 5. These were then used to calculate optical parameters that allow the retrieval of ash mass loadings from the Infrared Atmospheric Sounding Interferometer (IASI) satellite data using the optimal estimation algorithm of Ventress et al. (2016). IASI is a nadir-viewing Fourier Transform Spectrometer measuring in the infrared (3.62–15.5 μm). Briefly, Ventress et al. (2016) implement an iterative optimal estimation retrieval algorithm to produce probable values for volcanic ash properties. Combining an infinitely thin (geometrically) ash plume with a fast radiative transfer model to simulate the ash plume, and analyzing the spectra from IASI, the scheme is able to retrieve the following parameters: ash optical depth (at a reference wavelength of 550 nm), ash effective radius (μm), ash plume top height (km), and brightness temperature (K), which can be used to infer the mass loading of the plume. The results were compared with retrievals based on the Eyjafjallajökull ash refractive index used by Ventress et al. (2016). An objective cost function, detailed in Ventress et al., 2016, was used to determine whether using the calculated refractive indices provides an improvement over the use of a measured index of a different ash composition.

3. Volcanic Ash Compositions

Bulk ash major oxide compositions determined by XRF are reported in Table 2, together with the specific ferric/ferrous iron ratios (*f*) used for the NBO/T calculation. Glass major oxide compositions determined by EPMA are reported in Table 3. The suite of samples covers a wide compositional range from basalt to rhyolite (Figure 1). Bulk SiO_2 content ranges from 48.0 to 74.9 wt.%, and total alkalis ($Na_2O + K_2O$) range from 3.36 to

Table 2

Major Oxide Composition of Bulk Ash in wt.% Determined by XRF

Sample	SiO$_2$	TiO$_2$	Al$_2$O$_3$	Fe$_2$O$_3$[a]	MnO	MgO	CaO	Na$_2$O	K$_2$O	P$_2$O$_5$	SO$_3$	LOI	Total	f	NBO/T
Askja	72.35	0.86	12.58	4.01	0.113	0.86	2.62	4.05	2.373	0.171	<0.003	1.02	99.10	0.50	0.13
Aso	54.96	0.85	18.30	7.95	0.126	3.48	8.55	2.77	1.699	0.239	1.083	2.88	99.34	0.30	0.43
Augustine	62.86	0.62	16.58	5.08	0.111	3.10	6.48	3.92	1.103	0.123	<0.003	0.16	100.44	0.35	0.26
Chaitén	74.90	0.16	14.15	1.47	0.063	0.35	1.54	4.28	3.025	0.063	<0.003	1.33	99.23	0.50	0.04
Etna[b]	48.04	1.79	17.80	10.43	0.175	5.28	10.08	3.67	2.087	0.585	0.058	−0.09	99.18	0.30	0.63
Eyjafjallajökull (a)	60.00	1.31	14.68	8.22	0.216	2.93	4.47	5.64	2.283	0.240	0.006	−0.08	98.28	0.40	0.38
Eyjafjallajökull (b)	58.85	1.46	14.96	8.51	0.209	3.32	5.01	5.36	2.059	0.260	<0.003	−0.16	99.39	0.40	0.40
Grimsvötn (a)	50.58	2.81	13.59	13.46	0.212	5.57	9.94	2.87	0.488	0.305	0.163	−0.93	98.21	0.20	0.74
Grimsvötn (b)	50.33	2.91	13.58	13.71	0.218	5.32	9.86	2.89	0.479	0.312	0.387	−0.42	98.67	0.20	0.75
Nisyros	74.16	0.33	14.01	2.24	0.096	1.02	1.59	2.65	3.803	0.087	0.016	4.85	99.02	0.40	0.05
Okmok	53.23	1.22	16.75	9.84	0.186	5.15	9.33	3.22	0.880	0.181	0.004	−0.13	100.06	0.30	0.54
Spurr	55.99	0.73	18.96	7.26	0.153	4.45	7.63	3.48	0.962	0.235	0.157	0.51	100.30	0.30	0.36
Tongariro	64.13	0.70	17.72	6.41	0.070	2.14	4.66	2.39	1.359	0.147	0.266	5.96	99.20	0.35	0.17

Note. LOI = loss on ignition; NBO/T = nonbridging oxygens to tetrahedrally coordinated cations; XRF = X-ray fluorescence. Results quoted as component oxide weight percent, recalculated on a volatile-free basis. Original totals include LOI. Specific ferric/ferrous ratios (*f*) used to calculate NBO/T are reported.
[a]Total iron expressed as Fe$_2$O$_3$.   [b]Sample underwent a two-stage ignition to avoid potential problems caused by the ash composition that may have engendered significant sintering or melting at 950 °C. First stage ignition was undertaken at 750 °C.

7.92 wt.%. Bulk NBO/T ranges from 0.04 to 0.79. Glass SiO$_2$ content ranges from 50.2 to 73.7 wt.%, and total alkalis (Na$_2$O + K$_2$O) from 3.08 to 9.54 wt.%. Glass NBO/T ranges from 0.03 to 0.76. This range is typical of the spectrum of volcanic ash compositions erupted from subduction-zone volcanoes, which are the dominant sources of volcanic ash globally (Cashman & Rust, 2016). Differences between bulk and glass compositions primarily reflect the mineral (crystal) content of the ash.

4. Correlations With Complex Refractive Index

4.1. Visible Wavelengths

The real and imaginary components of the refractive indices of the Ball et al. (2015) data set show a strong linear relationship with both the bulk and glass compositions (SiO$_2$ and NBO/T) at 450.0, 546.7, and 650 nm. The strength of the correlation, represented by R^2, varies with wavelength and shows differences between bulk and glass and between SiO$_2$ content and NBO/T. The correlation of the real part with bulk composition is shown in Figure 2, and with glass is shown in Figure 3. The real part appears to be more strongly correlated with bulk compositions than glass, with R^2 values for bulk SiO$_2$ (0.899–0.916) greater than those for

Table 3

Major Oxide Composition of Glassy Components in wt.% Determined by EPMA

Sample	SiO$_2$	TiO$_2$	Al$_2$O$_3$	FeO[a]	MnO	MgO	CaO	Na$_2$O	K$_2$O	P$_2$O$_5$	Total	n	f	NBO/T
Askja	73.69	0.77	12.79	3.24	0.10	0.60	2.46	3.81	2.406	0.136	98.35	24	0.5	0.10
Aso	55.90	0.96	19.23	7.15	0.15	2.22	8.69	3.26	2.182	0.274	98.90	57	0.3	0.32
Augustine	66.20	0.24	19.94	1.29	0.04	0.20	6.49	4.27	1.259	0.072	100.18	30	0.4	0.04
Chaitén	73.70	0.11	15.50	1.09	0.06	0.22	2.31	4.40	2.562	0.043	98.89	30	0.5	0.05
Etna	50.92	2.02	16.64	10.25	0.24	3.30	7.47	4.58	3.817	0.769	97.87	25	0.35	0.55
Eyjafjallajökull (a)	66.43	0.93	14.14	5.93	0.18	0.65	1.98	5.84	3.696	0.234	99.38	15	0.5	0.21
Eyjafjallajökull (b)	64.25	1.18	14.81	6.52	0.18	1.00	3.01	5.54	3.199	0.312	98.89	35	0.5	0.24
Grímsvötn (a)	51.30	2.80	13.37	13.33	0.23	5.56	9.81	2.75	0.483	0.363	98.48	14	0.2	0.76
Nisyros	72.20	0.23	16.34	1.48	0.05	0.15	3.14	3.00	3.390	0.027	96.29	10	0.5	0.10
Okmok	55.19	1.68	14.10	11.82	0.22	4.03	8.05	3.41	1.213	0.283	97.65	27	0.3	0.59
Spurr	50.21	0.10	29.53	1.56	0.04	1.44	13.92	2.97	0.107	0.112	99.28	30	0.2	0.10
Tongariro	58.18	0.16	25.55	1.08	0.03	0.30	9.67	3.80	1.150	0.087	99.34	33	0.35	0.03

Note. EPMA = electron probe microanalyzer; NBO/T = nonbridging oxygens to tetrahedrally coordinated cations. Averages are based on *n* number of analyses. Results quoted as component oxide weight percent, normalized to 100% with original totals reported. Specific ferric/ferrous ratio (*f*) used to calculate NBO/T is reported.
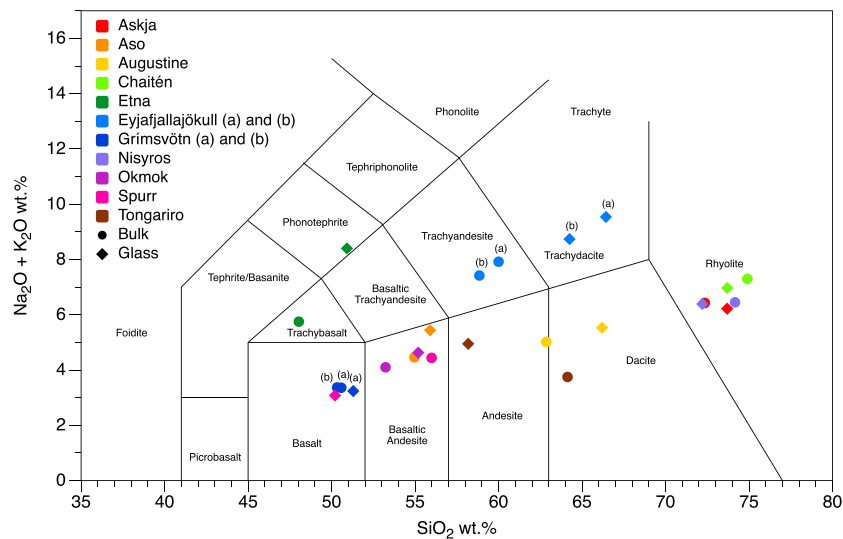[a]Total iron expressed as FeO.

Figure 1. Total alkalis versus silica diagram after Le Maitre et al. (2002). Bulk analyses for each sample are represented by circles, and glass analyses are represented by diamonds. Sample details are presented in Table 1, and composition data in Tables 2 and 3.

glass SiO_2 (0.756–0.789). This same trend can be seen for NBO/T, with R^2 values for bulk (0.963–0.969) greater than the R^2 values for glass (0.801–0.828). Figure 4 shows that the imaginary part has a stronger correlation with bulk SiO_2 (R^2 = 0.802–0.857) than with bulk NBO/T (R^2 = 0.643–0.811). Similarly, the glass SiO_2 (R^2 = 0.786–0.824) is better correlated with the imaginary part than the glass NBO/T (R^2 = 0.456–0.702), shown in Figure 5. The correlation for the imaginary part with NBO/T (glass and bulk) gets weaker as wavelength increases, whereas this trend is not observed for SiO_2. Correlation with the imaginary part appears to be weaker in general than with the real part, and correlations with bulk compositions appear to be stronger than with glass, with the exception of glass SiO_2 for the imaginary part, which is similar to that of the bulk.

The higher R^2 for bulk composition is likely due to the measurement technique used by Ball et al. (2015). It was undertaken on a grain-by-grain basis with little discrimination between grain types, and so it represents an average of the whole sample as opposed to just the glassy component. The key difference between SiO_2 and NBO/T as compositional parameters is that the latter is a measure of the depolymerization of the tetrahedral structure within the melt, which affects the length of T–O⁻ bonds. We do not expect to see much difference between SiO_2 and NBO/T correlations in the visible range because variations in bond length are only observable in the infrared region, where silicate bond vibrations are detectable. The very high correlations with the real part indicate that SiO_2 content is primarily influencing the scattering. SiO_2 content is the main control on NBO/T because it is the most abundant tetrahedral cation, which explains why NBO/T is also strongly correlated with n. Poorer correlation with the imaginary part may be due to the fact that absorption in the visible region is influenced by electronic processes, such as crystal field effects (Clark, 1999) caused by unfilled electron shells of transition elements (Ni, Cr, Co, Fe, etc.). It is not directly affected by the SiO_2 content or tetrahedral network. In addition, silicate glass is transparent in the visible range (Kitamura et al., 2007), meaning any absorption is due to other elements. The correlation is likely due to the indirect effect of SiO_2 content on the proportion of mafic minerals containing these transition metals.

4.2. Broad-Spectrum Correlations

To explore the relationships between refractive indices and composition at other wavelengths, we compared the complex refractive indices from Reed et al. (2018) with our composition measurements. A linear regression analysis at each measurement wavelength (0.4–19 μm) was used to determine R^2 for the correlation with bulk and glass composition in terms of SiO_2 and NBO/T (Figure 6). For the real part, this produces high R^2 values (Figure 6) in the visible to near-infrared range (0.4–3.5 μm) for each of the four compositional
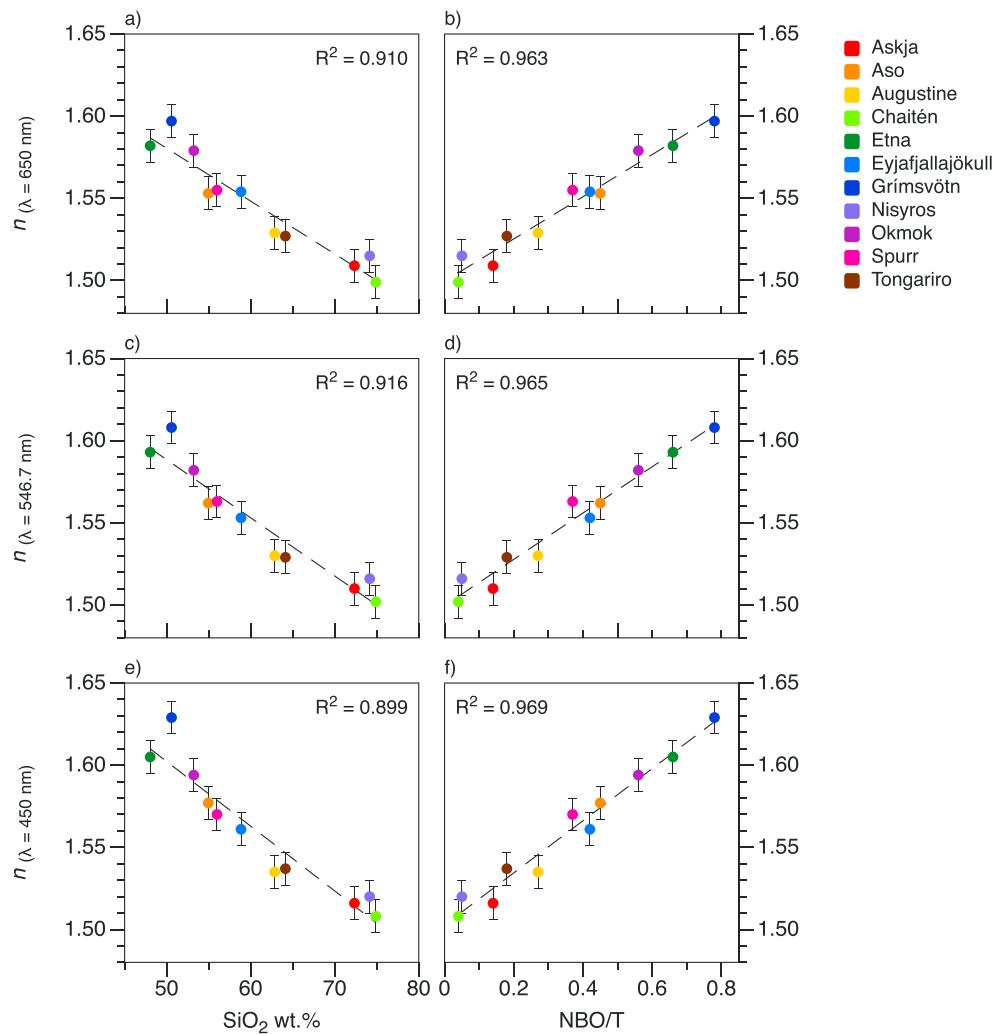
Figure 2. Real part of the refractive index (n) versus ash sample bulk SiO_2 and bulk nonbridging oxygens to tetrahedrally coordinated cations (NBO/T). Plots (a) and (b) are for n measured at a wavelength of 650 nm, (c) and (d) are at 546.7 nm, and (e) and (f) are at 450 nm.

parameters: bulk SiO_2 ($R^2 > 0.8$), glass SiO_2 ($R^2 > 0.6$), bulk NBO/T ($R^2 > 0.9$), and glass NBO/T ($R^2 > 0.7$). In this region (0.4–3.5 μm), scattering dominates the interaction between light and particles. This is consistent with results from section 4.1 and shows that the linear relationship extends to longer wavelengths. R^2 varies greatly in the midinfrared range (3.5–18 μm) and decreases dramatically around 6 μm, where n begins to show greater structure (lower panel, Figure 6). Only glass SiO_2 R^2 remains above 0.5 between 6 and 8 μm. Within the IASI spectral range of 3.62–15.5 μm, local peaks in R^2 for each of the four compositional parameters occur around 8, 10, and 12 μm. Between 8 and 12 μm these precede the turning points in n, occurring at slightly shorter wavelengths. The dips in R^2 correspond to the broader trough (8.5–9 μm) and peak (around 11 μm), where the measurements of n intersect one another, indicating that the relationship with composition at these wavelengths is nonlinear. Bulk R^2 values (solid line, Figure 6) are higher than glass R^2 (dashed line, Figure 6) over most of the spectral range for the real part, except between 5–9.5 μm and 10–11 μm for SiO_2, where glass R^2 is higher.

The correlation is very poor (R^2 close to zero) for the imaginary part in the visible to near-infrared region (Figure 7), contrary to the findings in section 4.1 with the visible measurements. This is likely due to the difference in measurement techniques between Ball et al. (2015) and Reed et al. (2018), who used much finer-grained samples with effective radii ranging from 0.574 to 1.16 μm. At wavelengths below 7 μm,
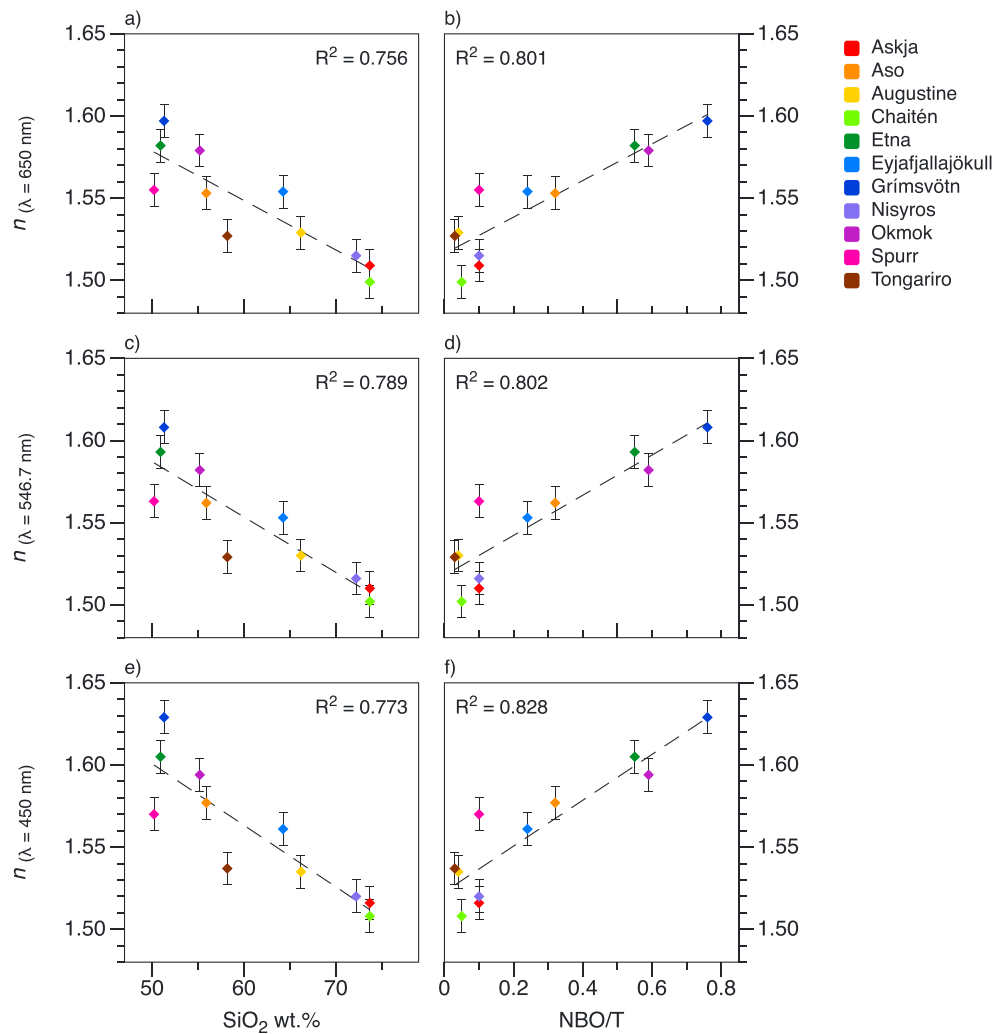
Figure 3. Real part of the refractive index (n) versus ash sample glass SiO_2 and glass nonbridging oxygens to tetrahedrally coordinated cations (NBO/T). Plots (a) and (b) are for n measured at a wavelength of 650 nm, (c) and (d) are at 546.7 nm, and (e) and (f) are at 450 nm.

Reed et al. (2018) reported greater uncertainties on the measured mass extinction coefficient from which the complex refractive index was retrieved. At shorter wavelengths (0.4–7 μm) scattering dominates the interaction, but as the wavelength of the incident light becomes larger than the particle size (>7 μm), scattering efficiency is reduced, and absorption begins to dominate. This effect can clearly be seen in Figure 7 where R^2 begins to increase at wavelengths above 7 μm. The T–O⁻ bond absorption feature occurs at around 8–12 μm depending on its length (Kieffer, 1979), governed by the nature of cations forming the tetrahedral framework (Mysen & Richet, 2005). In this data set, k peaks between 9 and 10 μm, corresponding to the asymmetric stretching resonance of the Si–O–Si bridge in silicates (Kitamura et al., 2007). This feature shifts to longer wavelengths as the bonds become longer, so we would expect to see a lower frequency absorption peak in samples with a greater NBO/T. The dip in correlation (R^2) between 3.5 and 4 μm is in agreement with spectroscopic studies on silica glass that show that it is effectively opaque at this wavelength (Kitamura et al., 2007). R^2 peaks at around 8.3 and 11.5 μm, either side of this absorption peak. The peaks in k vary in width and intensity, and according to wavelength, so the linear relationship breaks down where the spectra intersect, and this detail is not captured in our parameterization in section 5. Bulk composition (solid line, Figure 7) produces higher R^2 values than glass (dashed line, Figure 7) for NBO/T and over most of the spectrum for SiO_2, except in the range of 8–9 μm where glass SiO_2 has a higher R^2.
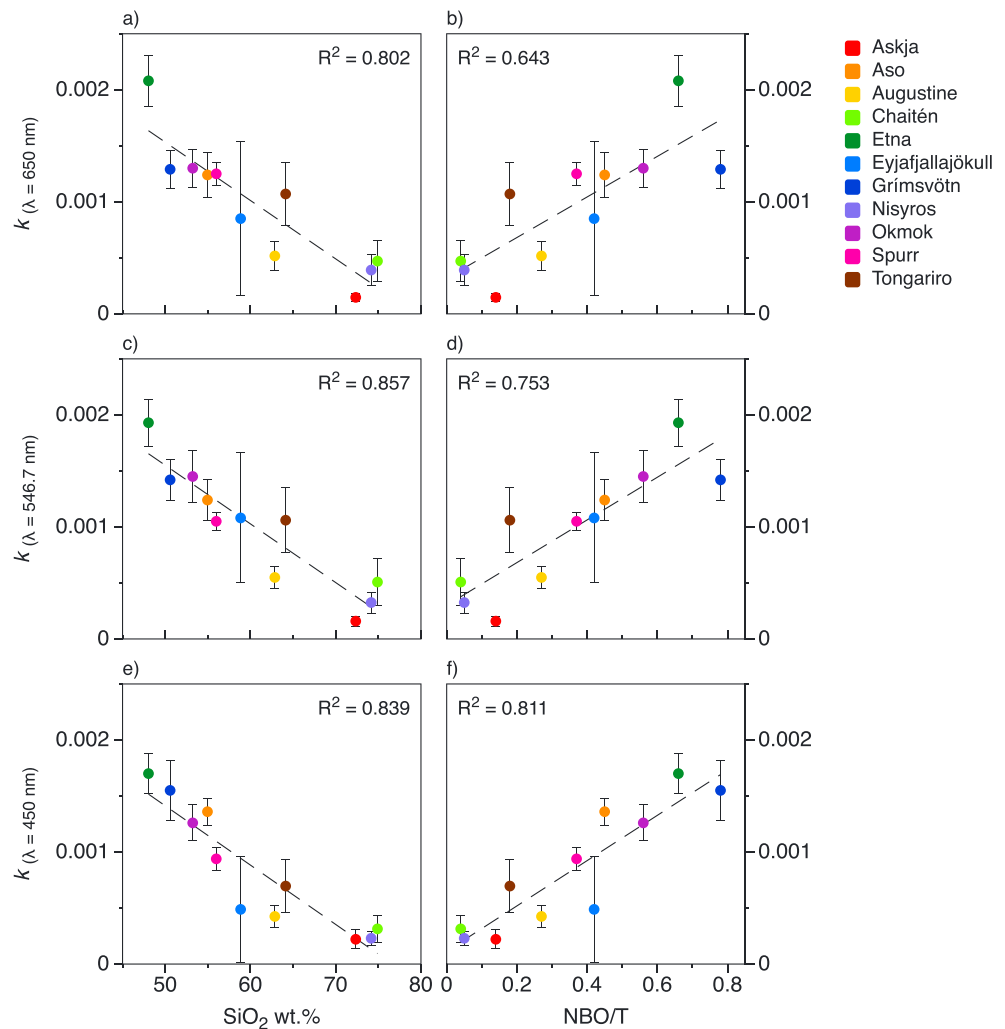
Figure 4. Imaginary part of the refractive index (k) versus ash sample bulk SiO_2 and bulk nonbridging oxygens to tetrahedrally coordinated cations (NBO/T). Plots (a) and (b) are of k measured at a wavelength of 650 nm, (c) and (d) are at 546.7 nm, and (e) and (f) are at 450 nm.

5. Parameterization

The variability in R^2 across the spectrum and the location of the peaks in R^2 around the important spectral shape features (peaks and troughs) in both parts of the complex refractive index mean that there is enough information to allow us to make justifiable estimates of n and k based on composition alone. The broad-spectrum correlations indicate that using bulk ash composition gives overall higher R^2 values than using the glass composition, so we have based our parameterization on bulk composition. The parameterization used is a linear regression with bulk NBO/T and SiO_2 as the input variables and the real (n_i) and imaginary parts (k_i) of the complex index of refraction as the outputs. There are M wavelengths, spaced irregularly, and the regression equations are

$$n_{ij} = a_{ij} + b_{ij} X_j, \qquad (2)$$

and,

$$k_{ij} = c_{ij} + d_{ij} X_j, \qquad (3)$$

where a_i, b_i, c_i, and d_i are regression coefficients provided at discrete wavelengths λ_i, $i = 1 \ldots M$. X_j is the fraction NBO/T when $j = 1$ and the $\%SiO_2$ when $j = 2$. The coefficients are tabulated at each wavelength and provided as a spreadsheet in Data Set S2.

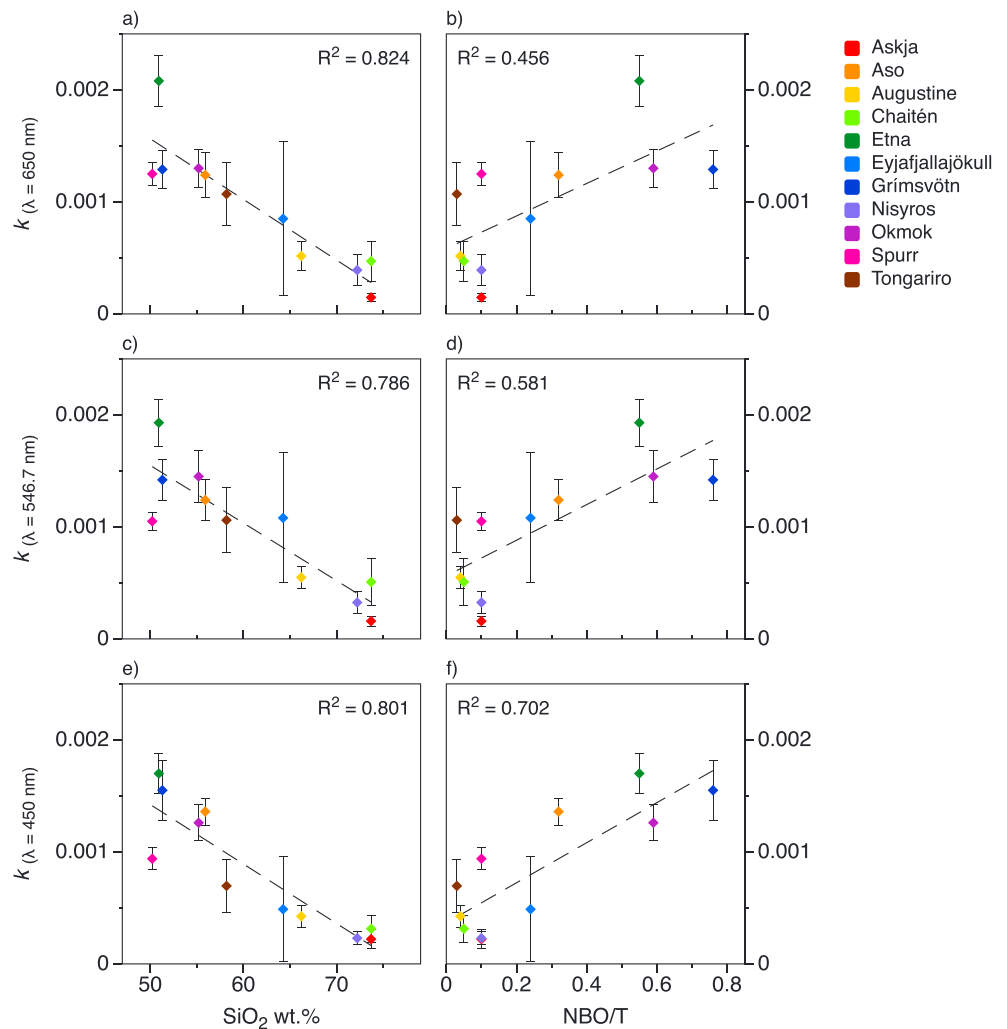**Figure 5.** Imaginary part of the refractive index (k) versus ash sample glass SiO_2 and glass nonbridging oxygens to tetrahedrally coordinated cations (NBO/T). Plots (a) and (b) are of k measured at a wavelength of 650 nm, (c) and (d) are at 546.7 nm, and (e) and (f) are at 450 nm.

Figure 8 shows the effect of varying the NBO/T and SiO_2 input parameters on the calculated complex refractive index. Using NBO/T (Figure 8a) in the parameterization results in a slight dampening of the amplitude of the curve generated for n when compared with using SiO_2 (Figure 8b). Between 9.2–10.4 μm and 11.2–12.8 μm the variation of n with increasing SiO_2 content is greater than the variation in NBO/T, so the parameterization is more sensitive to differences in SiO_2 than NBO/T in these regions. Similar effects are noted in the imaginary part, with a smaller variation in k between 10 and 11.8 μm for NBO/T (Figure 8c) than for SiO_2 (Figure 8d). Increasing the NBO/T results in a higher peak in k when compared with the variation in peak height for changing SiO_2 content. In the measurement data set the height of the peak in k does not appear to vary according to SiO_2 or NBO/T, so there may be other factors, such as variations in particle shape between samples, which have affected the measurements of extinction and scattering used to retrieve the complex refractive index (Reed et al., 2018). The peak in k in the parameterization also shifts to longer wavelengths and broadens as SiO_2 content decreases and as NBO/T increases, which is consistent with what would be expected due to lengthening of T–O⁻ bonds. There are certain wavelengths (e.g., 10.5 μm) at which the model will return the same refractive index regardless of the composition. This is a consequence of imposing a linear regression at every wavelength on a nonlinear spectrum and is a limitation of the method. Essentially, the R^2 value goes to zero at these points, so the linear fit will have no gradient (i.e., horizontal line) and return the same value of the refractive index for all compositions. Calculating the refractive index for compositions
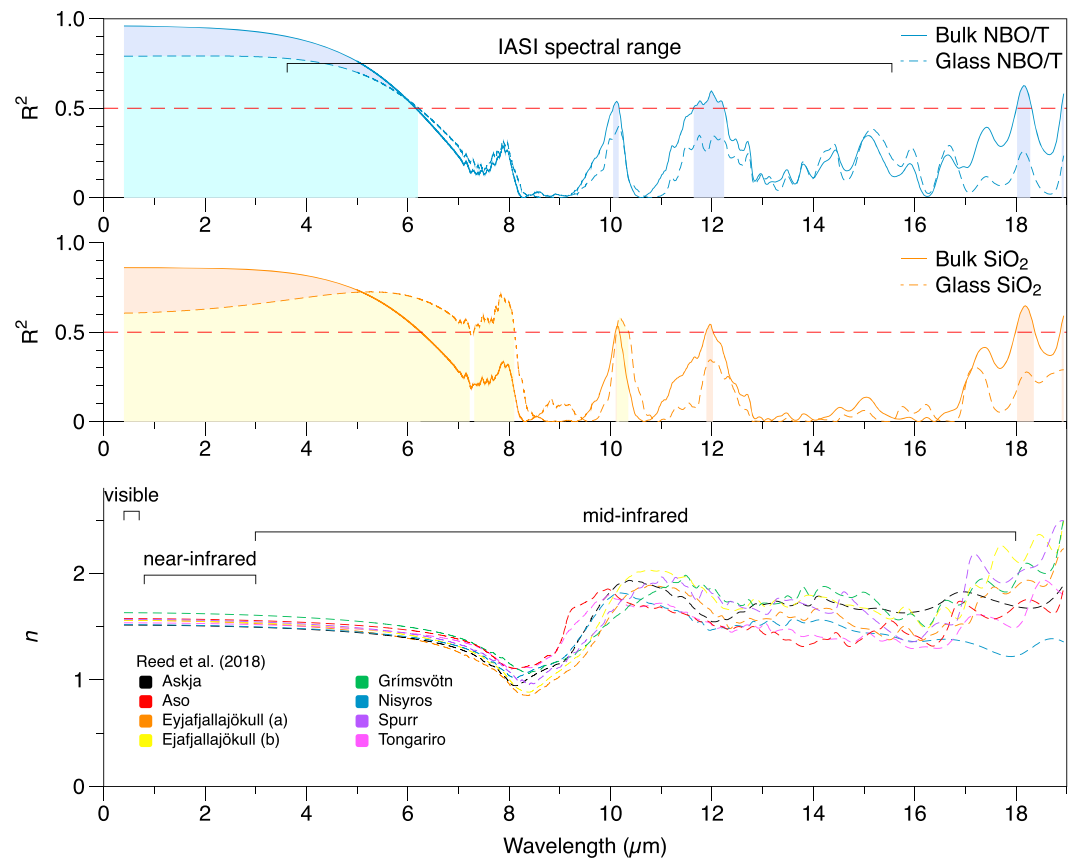
Figure 6. R^2 for the linear regressions between the real part of the refractive index (n) and ash sample nonbridging oxygens to tetrahedrally coordinated cations (NBO/T; upper panel) or SiO_2 (middle panel) versus wavelength of measurement. The n measurements are from Reed et al. (2018) and are represented by colored dashed lines (lower panel). R^2 values for the correlation between n and bulk ash composition are represented by the solid lines and for the correlation between n and glass composition by the dashed lines. Shading under the curves shows the areas where $R^2 > 0.5$, with the darker shade representing bulk and lighter shade glass. The Infrared Atmospheric Sounding Interferometer (IASI) spectral range is also indicated.

outside of the measured range assumes a continuation of the line of best fit at the specified wavelength. The fluctuations at wavelengths >11 μm highlight parts of the spectrum where the regression model is reflecting a greater sensitivity to changes composition; that is, it is fitting a linear model with a steeper gradient. Referring back to Figures 6 and 7, one can see that the R^2 values are >0.5 over a wider range for NBO/T than for SiO_2 for both n and k, so greater confidence can be given to the NBO/T model. The bulk NBO/T appears, on balance, to be the best parameter to represent composition. For this reason, and for ease of modeling, the subsequent analyses have been undertaken using the bulk NBO/T parameter.

In order to assess how well the parameterization performs at reproducing an independent data set, we compared it to the real and imaginary parts of the Pollack data set. Compositional data from Pollack et al. (1973) were used to calculate the NBO/T for the five samples reported: "Obsidian Little Glass Mt." (Obsidian 1), "Obsidian Lake County" (Obsidian 2), "Basaltic glass" (Basalt 1), "Basalt" (Basalt 2), and "Andesite." The calculated indices generally show good agreement with the measurements for both parts of the refractive index, broadly capturing the shape and alignment of the curves (Figure 9). The parameterization underestimates the peaks and overestimates the troughs of n to varying degrees. This is more evident for the two obsidian samples, and agreement is better for the two basalt samples and the andesite sample. For the imaginary part the parameterization underestimates the main peak between 8 and 12 μm. Again, this is more pronounced for the two obsidian samples than the basalt and andesite samples. At wavelengths greater than 12 μm, the calculated k fits the measurements better for the two obsidian samples than the other three samples.
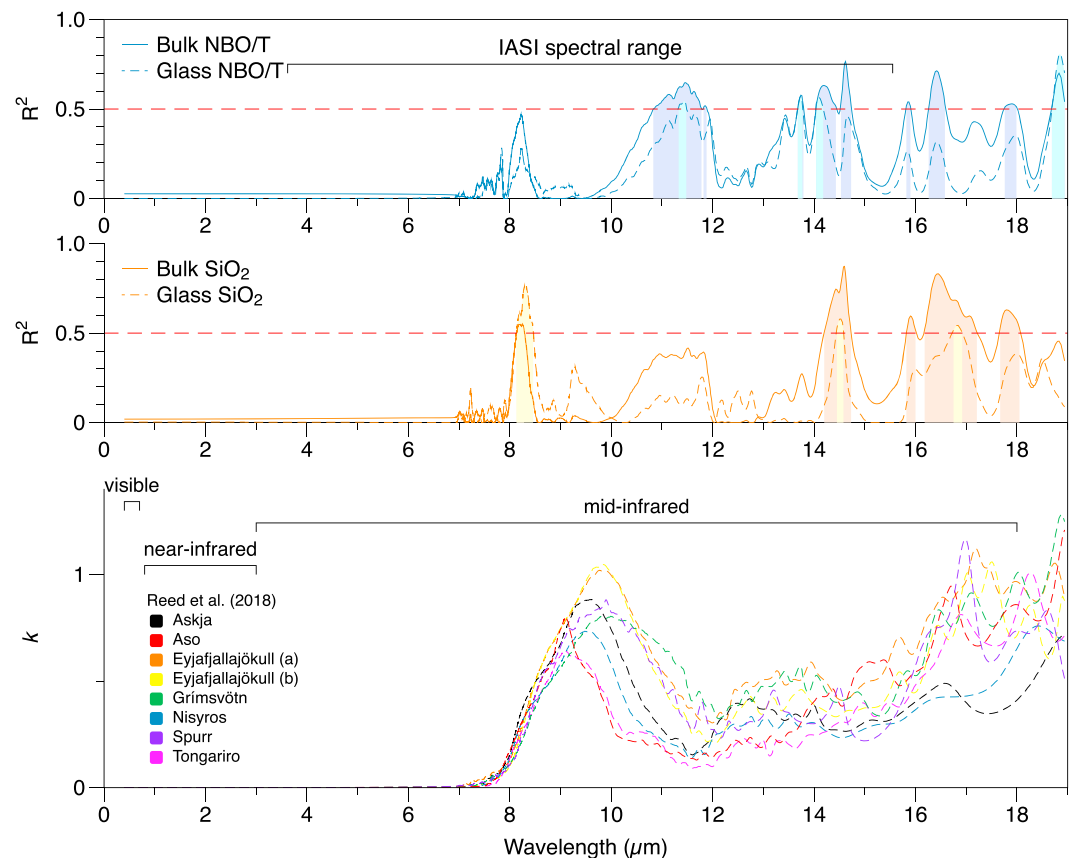
Figure 7. R^2 for the linear regressions between the imaginary part (k) and ash sample nonbridging oxygens to tetrahedrally coordinated cations (NBO/T; upper panel) or SiO_2 (middle panel) versus wavelength of measurement. The k measurements are from Reed et al. (2018) and are represented by colored dashed lines (lower panel). R^2 values for the correlation between k and bulk ash composition are represented by the solid lines, and glass composition is represented by the dashed lines. Shading under the curves shows the areas where $R^2 > 0.5$, with the darker shade representing bulk and lighter shade glass. The Infrared Atmospheric Sounding Interferometer (IASI) spectral range is also indicated.

The difference in peak height in k may be due to differences in the nature of our samples compared with those of Pollack et al. (1973), with compositional heterogeneity between grains potentially affecting the measurements on which the parameterization was based. Measurements made on slabs rather than particulates are not subject to the same grain-size and shape effects as in our data set, and Reed et al. (2018) noted that variation particle shape between samples was not taken into account. For a discussion on how nonsphericity can affect the retrieval of complex refractive index, see Dubovik et al. (2002). As more ash refractive indices become available, their fit to the parameterization should be assessed, and if necessary, this new data should be added to the parameterization spreadsheet to update the model (Data Set S2). Despite linearly fitting the real and imaginary parts of the refractive index independently of one another, the parameterization still obeys the Kramers-Kronig relation (Bohren & Huffman, 1983) as well as it does for the original measurements on which it was based. The Kramers-Kronig relation shows that the real part of the refractive index can be derived if the imaginary part is known or vice versa. Using a parameterized k to calculate n via the relation results in a maximum difference of 2% and an average difference of 1% between that and the independently calculated n (via the parameterization).

5.1. Impact on Brightness Temperatures

Passive remote-sensing instruments measure radiances, which are a function of wavelength, from the atmosphere and surface. Radiative transfer through a substance in the atmosphere (e.g., volcanic ash cloud) is governed by the complex refractive index of that substance, and this can be utilized to calculate its physical properties, such as mass loading. In order to compare measurements at different wavelengths, the
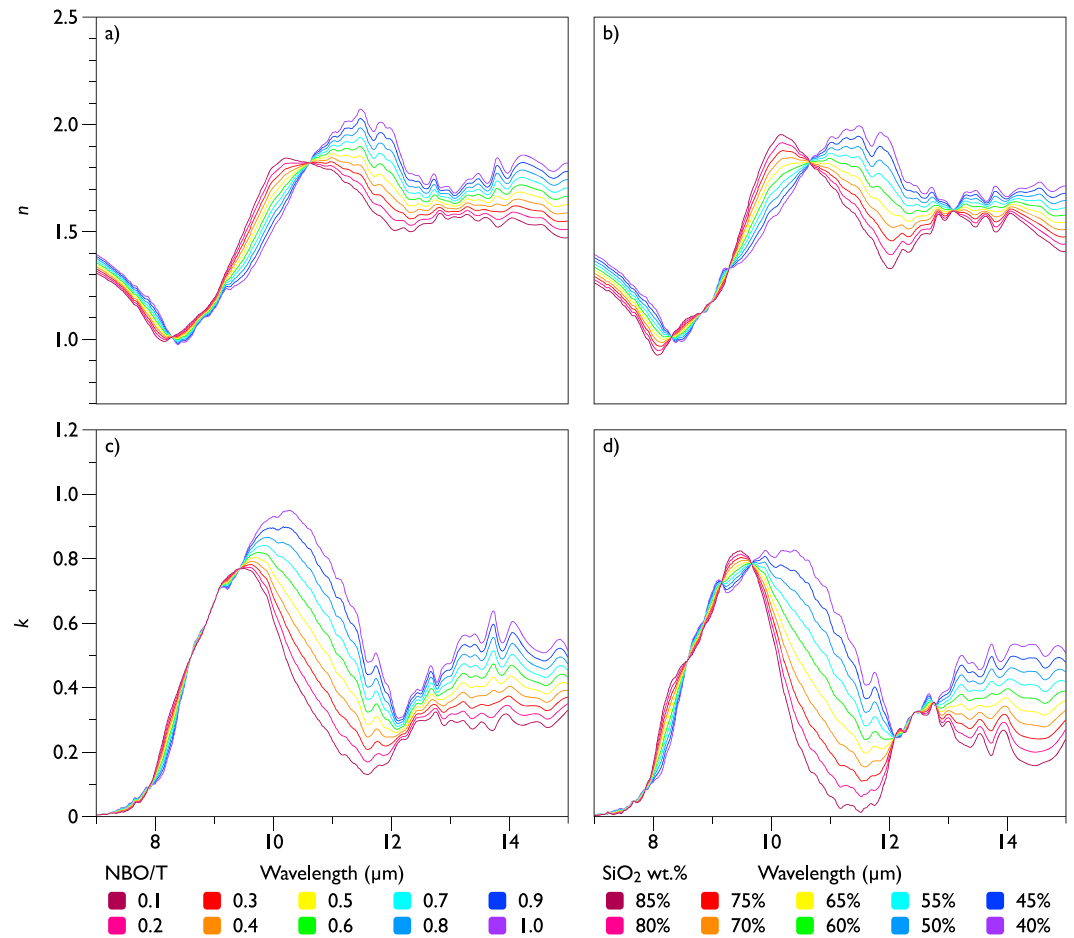
Figure 8. Modeled complex refractive indices showing the effect of varying parameters nonbridging oxygens to tetrahedrally coordinated cations (NBO/T) and SiO_2. (a) Modeled real part of the refractive index (n) based on NBO/T and (b) based on SiO_2 content. (c) Modeled imaginary part of the refractive index (k) based on NBO/T and (d) based on SiO_2 content. Typical bulk volcanic ash samples are most likely to have SiO_2 contents from 48 to 77 wt%; higher SiO_2 contents would only be expected in samples that have been enriched in quartz grains.

radiances must be converted to brightness temperatures, which are calculated by inverting the Planck function. Francis et al. (2012) showed that the choice of refractive index can have a significant effect on calculations of mass loading, derived from brightness temperature differences (Prata, 1989), so we have used our parameterization to investigate this potential impact. Differences between the parameterization and measured complex refractive indices at 10.5 and 11.5 μm of Pollack et al. (1973) are up to ±20%, as illustrated in Figure 9.

The impact on brightness temperature from errors in the estimation of k can be assessed using the expression for the brightness temperature difference provided by equation 5 of Prata and Grant (2001):

$$\Delta T = \Delta T_c \left(X - X^\beta \right), \tag{4}$$

$$X = 1 - \frac{\Delta T_{11}}{\Delta T_c}, \tag{5}$$

where ΔT is the brightness temperature difference, ΔT_c is the temperature difference between the cloud top and the surface (sometimes referred to as the thermal contrast), ΔT_{11} is the difference between the surface temperature and the brightness temperature measured at 11 μm, and β is the ratio of absorption coefficients (α) at two different wavelengths (λ), typically 12 and 11 μm. This expression relates the brightness
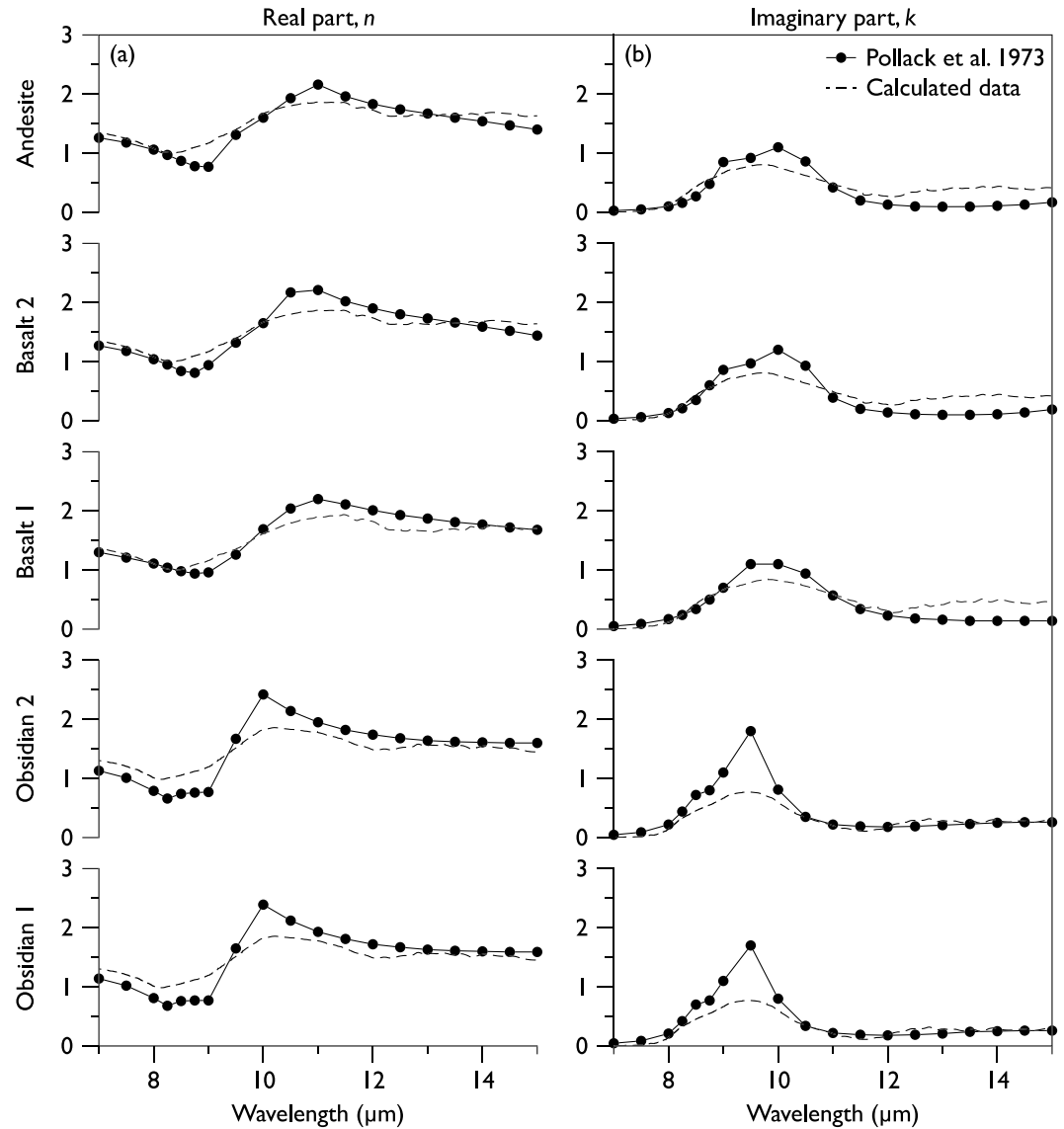
Figure 9. Complex refractive indices calculated from the parameterization compared with the measured indices from Pollack et al. (1973) for five different rock types: "Obsidian Little Glass Mt." (obsidian 1), "Obsidian Lake County" (obsidian 2), "basaltic glass" (basalt 1), "basalt" (basalt 2), and "andesite." (a) Real part (n); (b) imaginary part (k).

temperature difference as a function of the ratio of absorption coefficients (α_{12}/α_{11}). Noting that k can be expressed in terms of α (Prata & Prata, 2012) and after a little manipulation,

$$\alpha = \frac{4\pi}{\lambda} k_i(\lambda), \tag{6}$$

$$\beta = \frac{11}{12}\frac{k_{12}}{k_{11}}, \tag{7}$$

$$\delta(\Delta T) = \tau\,\delta\beta, \tag{8}$$

where τ is a scaling factor that includes the thermal contrast between the cloud top temperature and the brightness temperature at 12 μm and $\delta\beta$ is proportional to the change in the ratio of the imaginary parts of the refractive index at 12 and 11 μm. The mean difference between the parameterization and measured Pollack et al. (1973) ratios (k_{12}/k_{11}) is ±22%. An error analysis was performed using this model
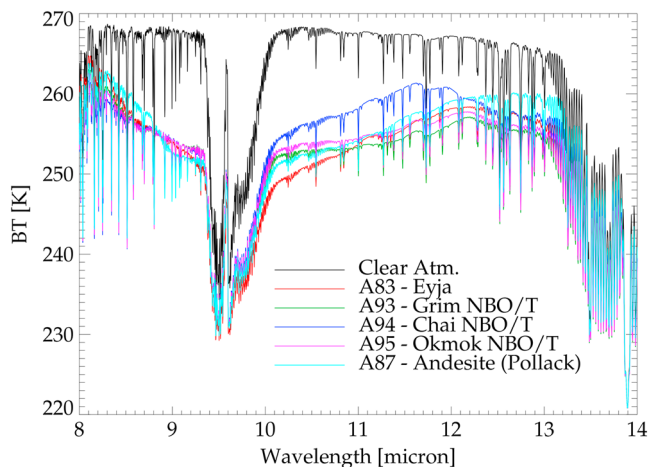
Figure 10. Brightness temperature (BT) simulations for a clear atmosphere and ash-contaminated atmosphere for each data set: A83 (Eyja), A93 (Grímsvötn), A94 (Chaitén), A95 (Okmok), and A87 (Pollack Andesite) with AOD = 1.00, R_{eff} = 5.00, and P = 400 hPa. NBO/T = nonbridging oxygens to tetrahedrally coordinated cations.

(equation (8)) by generating random samples (30,000 trials) of the ratios with perturbations in each k of ±20%, as suggested from Figure 9. To account for measurement errors, an additional perturbation of ±3% was included. The standard deviation of the distribution of δ (ΔT) due to measurement errors was found to be ~0.2 K, which is close to the measurement noise of current infrared satellite-based sensors. The standard deviation of the distribution due to perturbations of ±20% in each k value was between 1.5 and 3 K, demonstrating that errors in the refractive indices significantly impact brightness temperature differences, and therefore also mass loading. The impact on the retrieval of mass loading is more complicated, but see Figure 10 of Clarisse and Prata (2016), which shows mass loading as a function of brightness temperature difference. Mass loading is retrieved from aerosol optical depth (AOD) and effective particle radius (R_{eff}). Clarisse and Prata (2016) explain that for small particles, R_{eff} has the greatest influence on the mass loading, whereas once R_{eff} goes beyond a certain size (>30-μm diameter) AOD is more important. Wen and Rose (1994) suggest that for small particles the precise values of n and k are not too serious for mass loading retrievals. Essentially, our analysis shows that precision errors in the parameterization are within measurement noise, but accuracy, that is, incorrect choice of refractive index, can have a significant impact on brightness temperature differences.

6. Satellite Retrievals

Using the NBO/T parameterization reported in section 5, we calculated refractive indices for Grímsvötn (labeled A93 in Figure 10), Chaitén (A94), and Okmok (A95) ash. We selected these eruptions from our suite of samples to span a range of compositions (see section 3) and because IASI data were available. Brightness temperature simulations using an AOD of 1, R_{eff} of 5 μm and atmospheric pressure (P) of 400 hPa have been generated for each of these data sets, along with that of a measured refractive index from Eyjafjallajökull (labeled A83 in Figure 10) presented in Ventress et al. (2016), the Pollack Andesite (A87), and a clear atmosphere. Figure 10 shows that there are significant differences between using the parameterized refractive indices and using the measurement index A83 (Eyja) and A87 (Pollack Andesite). Although the broad features are similar, the parameterized indices are clearly differentiated according to composition.

In order to assess the potential effects of our new parameterization on retrieval performance and outputs, we compared retrievals using our new refractive indices with those using the measured refractive index A83 (Eyja) using cost function as a minimization parameter, as described in Ventress et al. (2016). When using the outputs of our new parameterization, we observed good agreement with the measurement retrieval (A83) in terms of the shape and extent of the plumes in all three eruptions. Overall slightly higher mass loadings were observed with the calculated indices, and the change in cost function, the minimization parameter used by Ventress et al. (2016), varied over different parts of the plume in each eruption (Figures 11a–11f).

Retrievals for the May 2011 Grímsvötn eruption (Figures 11a and 11b) showed good agreement in the overall shape of the plume and similar range in mass loadings. The area of mass loadings greater than 5 g/m^2 expanded further west for A93 than the A83 retrieval. Positive changes in mass loading were observed over the southern part of the plume (Figure 11a), with little change to the north. The cost function mostly decreased in the middle part of the plume, where A93 showed increases in mass loading, and increased in the southernmost part (Figure 11b).

The shape of the eruption plume for Chaitén in May 2008 from A94 showed good agreement with the A83 retrieval. The mass loading increased in the south and decreased in the north (Figure 11c). Most significantly, mass loadings of greater than 2 g/m^2 were detected along the southern limb of the plume using the new parameterized refractive index A94, which were not detected using the A83 data set. This is consistent with other observations of the Chaitén eruption plume, indicating that most of the ash dispersed to the southeast over Argentina, with little or none to the north (Gangale et al., 2010). This change in distribution resulted in a
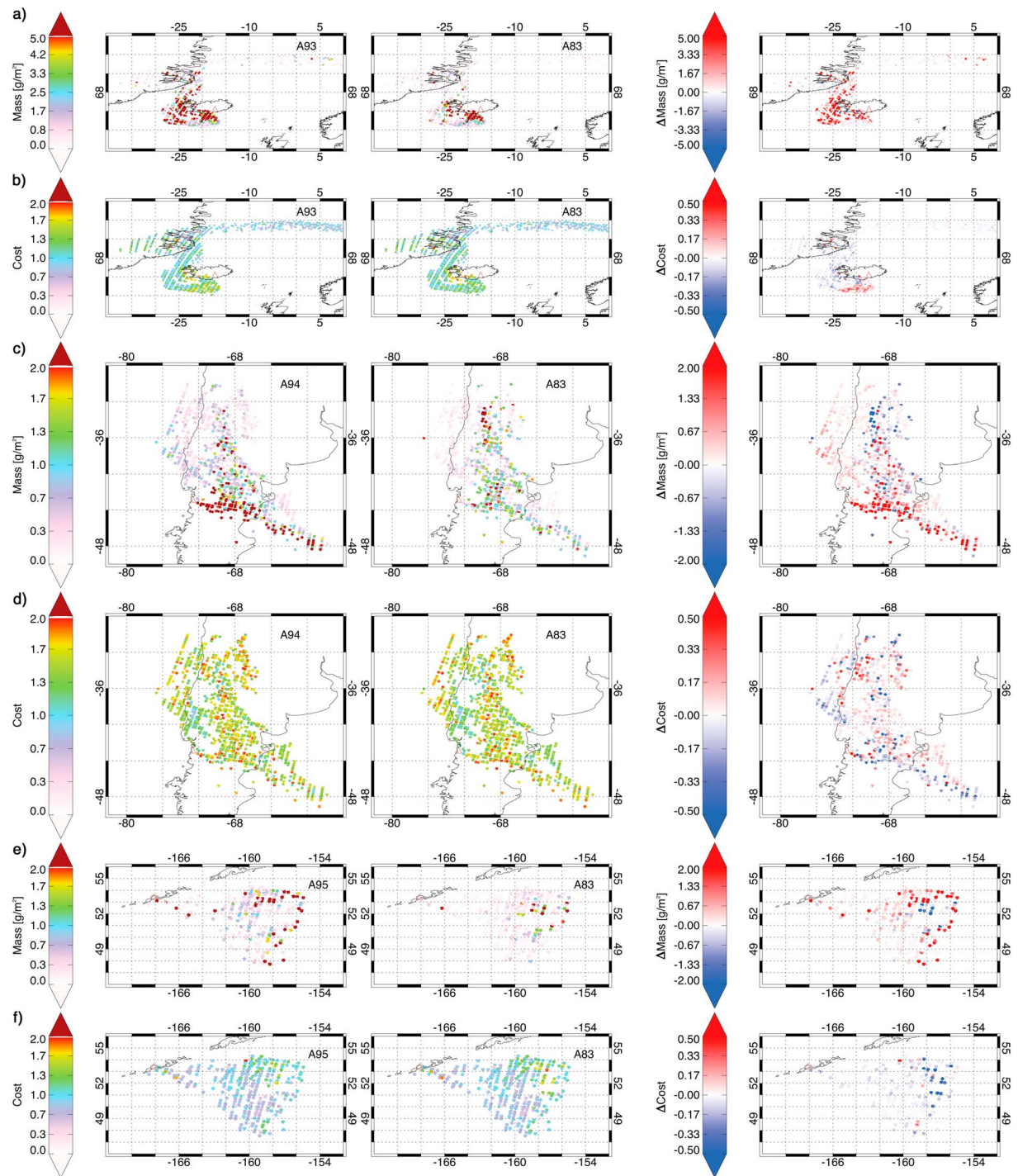
Figure 11. Satellite retrievals of mass loading from Infrared Atmospheric Sounding Interferometer data for the eruptions of Grímsvötn, Chaitén, and Okmok. The left-hand column is the retrieval using refractive indices calculated from our new parameterization (Grímsvötn—A93, Chaitén—A94, and Okmok—A95), the middle column uses a measured Eyjafjallajökull refractive index (A83), and the right-hand column is the difference between the two, that is, the first minus the second. (a) Mass loading and (b) cost function for Grímsvötn on 22 May 2011 in the afternoon, (c) mass loading and (d) cost function for Chaitén on 3 May 2008 in the morning, and (e) mass loading and (f) cost function for Okmok on 13 July 2008 in the morning.

decrease in cost function over the southernmost elongated part of the plume and an increase in cost to the north (Figure 11d). Additional retrievals for this eruption using the SiO_2 parameterization for reference are presented in Figures S1 to S4.

For the eruption of Okmok in July 2008, the plume was detected, fanning out east-southeast away from the volcano. The parameterized retrieval A95 picked up a slight shift in the distribution of mass loading. Greater mass was observed toward the outer parts of the plume and less toward the middle when compared with the A83 retrieval (Figure 11e). More pixels with mass loading greater than 2 g/m^2 were detected using the parameterized refractive index (A95) than with the Eyjafjallajökull measured refractive index (A83), and mass loadings were higher overall. The cost function decreased over the majority of the plume (Figure 11f), with the greatest reductions around the outer northeastern edge corresponding to the areas of increased mass.

One caveat with the retrieval algorithm is that it flags pixels containing either volcanic ash or SO_2 (previous works have used the presence of volcanic SO_2 as a proxy for the location of volcanic ash), so the algorithm may be attempting to fit the radiative transfer model to a scene that does not actually contain ash (Ventress et al., 2016). This can lead to large cost function values. We know, for example, that the SO_2 plume from the Grímsvötn eruption separated and dispersed northward while the majority of ash went southward (Prata et al., 2017). Nevertheless, the parameterized refractive indices make a significant difference compared with the Eyjafjallajökull ash measurements and, in the case of the Okmok eruption, clearly reduce the cost function.

7. Conclusions and Further Work

We have developed a method to estimate the complex refractive index of a volcanic ash sample based on its composition, in terms of silica content and/or NBO/T. A spreadsheet to calculate the complex refractive index using this new parameterization is provided in Data Set S2. We have demonstrated that glass chemistry does not represent the composition of these samples as well as the bulk chemistry, possibly indicating chemical heterogeneity down to very fine fractions. We find that it is sufficient to use wt.% SiO_2 to estimate refractive index but recommend that it is better to use NBO/T if the data are available. This simple linear model is an improvement on the current procedure of using a single standard reference refractive index data set, such as the Pollack "andesite," for all types of volcanic ash. By using an analytical expression, we have shown that errors of ±20% in the calculated imaginary part can have a significant effect on brightness temperature difference. Using this approach, we are able to produce retrievals of mass loadings that can replicate the broad features observed from IASI data using actual measured refractive indices of Eyjafjallajökull ash. We have also demonstrated that using a refractive index data set based on the eruption-specific composition does have an impact on the mass loading retrievals. In all three test cases we analyzed, the retrievals using our method were in good agreement, in terms of plume size and shape, with retrievals using the measured Eyjafjallajökull refractive index. However, slightly greater mass loadings were observed overall using our new ash refractive index parameterizations in the retrievals compared to using the Eyjafjallajökull refractive index, and the distribution of mass loadings and cost function varied significantly across the plumes. Mass loading is an important parameter used in volcanic ash dispersion modeling for estimating and forecasting ash concentrations downwind, which is a vital tool in assessing hazards for aviation (see Mackie et al., 2016, and references therein). The implication of our findings is that incorrect assumptions could lead to inaccurate mass loadings from satellite data, which is consistent with the findings of Francis et al. (2012) and Mackie et al. (2014). Our initial linear parameterization is a first approach to see if the method works, and future work would include further refinement through a more thorough characterization of compositional heterogeneity within samples. Further testing of the parameterization with new refractive index measurements as they become available in the midinfrared range (7–15 μm) will greatly improve its utility. Further ground truthing of quantitative satellite ash retrievals is also to be encouraged.

References

Ayris, P., & Delmelle, P. (2012). Volcanic and atmospheric controls on ash iron solubility: A review. *Physics and Chemistry of the Earth, Parts A/B/C*, *45-46*, 103–112. https://doi.org/10.1016/j.pce.2011.04.013

Ball, J. G. C., Reed, B. E., Grainger, R. G., Peters, D. M., Mather, T. A., & Pyle, D. M. (2015). Measurements of the complex refractive index of volcanic ash at 450, 546.7, and 650 nm. *Journal of Geophysical Research: Atmospheres*, *120*, 7747–7757. https://doi.org/10.1002/2015JD023521

Barton, I. J., Prata, A. J., Watterson, I. G., & Young, S. A. (1992). Identification of the Mount Hudson volcanic cloud over SE Australia. *Geophysical Research Letters*, *19*(12), 1211–1214. https://doi.org/10.1029/92GL01122

Bohren, C. F., & Huffman, D. R. (1983). *Absorption and scattering of light by small particles*. New York: John Wiley.

Casadevall, T. J. (1994). Volcanic ash and aviation safety: Proceedings of the first international symposium on volcanic ash and aviation safety. *US Geological Survey Bulletin*, *2047*, 1–6.

Cashman, K., & Rust, A. C. (2016). Volcanic ash: Generation and spatial variations. In S. Mackie, K. Cashman, H. Ricketts, A. C. Rust, & I. M. Watson (Eds.), *Volcanic ash: Hazard observation* (pp. 5–24). Amsterdam, Netherlands: Elsevier. https://doi.org/10.1016/B978-0-08-100405-0.00002-1

Clarisse, L., & Prata, A. J. (2016). Infrared sounding of volcanic ash. In S. Mackie, K. Cashman, H. Ricketts, & I. M. Watson (Eds.), *Volcanic ash: Hazard observation* (pp. 189–216). Amsterdam, Netherlands: Elsevier.. https://doi.org/10.1016/B978-0-08-100405-0.00017-3

Clarisse, L., Prata, A. J., Lacour, J.-L., Hurtmans, D., Clerbaux, C., & Coheur, P.-F. (2010). A correlation method for volcanic ash detection using hyperspectral infrared measurements. *Geophysical Research Letters*, *37*, L19806. https://doi.org/10.1029/2010GL044828

Clark, R. N. (1999). Spectroscopy of rocks and minerals, and principles of spectroscopy. In A. N. Rencz (Ed.), *Remote sensing for the earth sciences: Manual of remote sensing* (3rd ed., Vol. 3, pp. 3–52). New York: John Wiley and Sons, Inc.. https://doi.org/10.1111/j.1945-5100.2004.tb00079.x

Di Genova, D., Morgavi, D., Hess, K.-U., Neuville, D. R., Borovkov, N., Perugini, D., & Dingwell, D. B. (2015). Approximate chemical analysis of volcanic glasses using Raman spectroscopy. *Journal of Raman Spectroscopy*, *46*(12), 1235–1244. https://doi.org/10.1002/jrs.4751

Dubovik, O., Holben, B. N., Lapyonok, T., Sinyuk, A., Mishchenko, M. I., Yang, P., & Slutsker, I. (2002). Non-spherical aerosol retrieval method employing light scattering by spheroids. *Geophysical Research Letters*, *29*(10), 1415. https://doi.org/10.1029/2001GL014506

Francis, P. N., Cooke, M. C., & Saunders, R. W. (2012). Retrieval of physical properties of volcanic ash using Meteosat: A case study from the 2010 Eyjafjallajökull eruption. *Journal of Geophysical Research*, *117*, D00U09. https://doi.org/10.1029/2011JD016788

Gangale, G., Prata, A. J., & Clarisse, L. (2010). The infrared spectral signature of volcanic ash determined from high-spectral resolution satellite measurements. *Remote Sensing of Environment*, *114*(2), 414–425. https://doi.org/10.1016/j.rse.2009.09.007

Giordano, D., Russell, J. K., & Dingwell, D. B. (2008). Viscosity of magmatic liquids: A model. *Earth and Planetary Science Letters*, *271*(1–4), 123–134. https://doi.org/10.1016/j.epsl.2008.03.038

Grainger, R. G., Peters, D. M., Thomas, G. E., Smith, A. J. A., Siddans, R., Carboni, E., & Dudhia, A. (2013). Measuring volcanic plume and ash properties from space. In *Remote sensing of volcanoes and volcanic processes: Integrating observation and modelling*, *Special Publications* (Vol. 380, pp. 293–320). London: Geological Society. https://doi.org/10.1144/SP380.7

Harbin, M., Swanson, S., Nye, C., & Miller, T. (1995). Preliminary petrology and chemistry of proximal eruptive products; 1992 eruptions of Crater Peak, Mount Spurr Volcano, Alaska. In T. Keith (Ed.), *The 1992 eruptions of Crater Peak vent, Mount Spurr Volcano, Alaska, U. S. Geological Survey Bulletin 2139* (pp. 139–148).

Herbin, H., Pujol, O., Hubert, P., & Petitprez, D. (2017). New approach for the determination of aerosol refractive indices—Part I: Theoretical bases and numerical methodology. *Journal of Quantitative Spectroscopy and Radiative Transfer*, *200*, 311–319. https://doi.org/10.1016/j.jqsrt.2017.03.005

Jochum, K. P., Stoll, B., Herwig, K., Willbold, M., Hofmann, A. W., Amini, M., Aarburg, S., et al. (2006). MPI-DING reference glasses for in situ microanalysis: New reference values for element concentrations and isotope ratios. *Geochemistry, Geophysics, Geosystems*, *7*, Q02008. https://doi.org/10.1029/2005GC001060

Keller, J., Ryan, W. B. F., Ninkovich, D., & Altherr, R. (1978). Explosive volcanic activity in the Mediterranean over the past 200,000 yr as recorded in deep-sea sediments. *Geological Society of America Bulletin*, *89*(4), 591–604. https://doi.org/10.1130/0016-7606(1978)89<591:EVAITM>2.0.CO;2

Kieffer, S. W. (1979). Thermodynamics and lattice vibrations of minerals: 2. Vibrational characteristics of silicates. *Reviews of Geophysics*, *17*(1), 20–34. https://doi.org/10.1029/RG017i001p00020

Kitamura, R., Pilon, L., & Jonasz, M. (2007). Optical constants of silica glass from extreme ultraviolet to far infrared at near room temperature. *Applied Optics*, *46*(33), 8118–8133. https://doi.org/10.1364/AO.46.008118

Klüser, L., Erbertseder, T., & Meyer-Arnek, J. (2013). Observation of volcanic ash from Puyehue–Cordón Caulle with IASI. *Atmospheric Measurement Techniques*, *6*(1), 35–46. https://doi.org/10.5194/amt-6-35-2013

Krotkov, N. A., Flittner, D. E., Krueger, A. J., Kostinski, A., Riley, C., Rose, W., & Torres, O. (1999). Effect of particle non-sphericity on satellite monitoring of drifting volcanic ash clouds. *Journal of Quantitative Spectroscopy and Radiative Transfer*, *63*(2–6), 613–630. https://doi.org/10.1016/S0022-4073(99)00041-2

Larsen, J. F., Nye, C. J., Coombs, M. L., Tilman, M., Izbekov, P., & Cameron, C. (2010). Petrology and geochemistry of the 2006 eruption of Augustine Volcano. In J. A. Power, M. L. Coombs, & J. T. Freymueller (Eds.), *The 2006 eruption of Augustine Volcano* (Vol. 1769, pp. 335–382). Alaska: U.S. Geological Survey Professional Paper.

Larsen, J. F., Śliwiński, M. G., Nye, C., Cameron, C., & Schaefer, J. R. (2013). The 2008 eruption of Okmok Volcano, Alaska: Petrological and geochemical constraints on the subsurface magma plumbing system. *Journal of Volcanology and Geothermal Research*, *264*, 85–106. https://doi.org/10.1016/j.jvolgeores.2013.07.003

Le Maitre, R. W. (Ed.), Streckeisen, A., Zanettin, B., Le Bas, M. J., Bonin, B., Bateman, P., et al. (2002). *Igneous rocks: A classification and glossary of terms* (2nd ed.). Cambridge: Cambridge University Press.

Longchamp, C., Bonadonna, C., Bachmann, O., & Skopelitis, A. (2011). Characterization of tephra deposits with limited exposure: The example of the two largest explosive eruptions at Nisyros volcano (Greece). *Bulletin of Volcanology*, *73*(9), 1337–1352. https://doi.org/10.1007/s00445-011-0469-9

Mackie, S., Cashman, K., Ricketts, H., Rust, A. C., & Watson, I. M. (2016). In S. Mackie, K. Cashman, H. Ricketts, A. C. Rust, & I. M. Watson (Eds.), *Volcanic ash: Hazard observation*. Amsterdam, Netherlands: Elsevier.

Mackie, S., Millington, S., & Watson, I. M. (2014). How assumed composition affects the interpretation of satellite observations of volcanic ash. *Meteorological Applications*, *21*(1), 20–29. https://doi.org/10.1002/met.1445

Middlemost, E. A. K. (1989). Iron oxidation ratios, norms and the classification of volcanic rocks. *Chemical Geology*, *77*(1), 19–26. https://doi.org/10.1016/0009-2541(89)90011-9

Mills, K. C. (1993). The influence of strcuture on the physico-chemical properties of slags. *ISIJ International*, *33*(1), 148–155. https://doi.org/10.2355/isijinternational.33.148

Mysen, B. O., & Richet, P. (2005). *Silicate glasses and melts*. Amsterdam, Netherlands: Elsevier.

Mysen, B. O., Virgo, D., & Seifert, F. A. (1982). The structure of silicate melts: Implications for chemical and physical properties of natural magma. *Reviews of Geophysics*, *20*(3), 353. https://doi.org/10.1029/RG020i003p00353

Patterson, E. M. (1975). Optical absorption coefficients of soil aerosol particles and volcanic ash between 1 and 16 μm. *Second Conference on Atmospheric Radiation*, 177–180.

Patterson, E. M. (1981). Measurements of the imaginary part of the refractive index between 300 and 700 nanometers for Mount St. Helens ash. *Science*, *211*(4484), 836–838. https://doi.org/10.1126/science.211.4484.836

Patterson, E. M., Pollard, C. O., & Galindo, I. (1983). Optical properties of the ash from El Chichon volcano. *Geophysical Research Letters*, *10*(4), 317–320. https://doi.org/10.1029/GL010i004p00317

Pollack, J. B., Toon, O. B., & Khare, B. N. (1973). Optical properties of some terrestrial rocks and glasses. *Icarus*, *19*(3), 372–389. https://doi.org/10.1016/0019-1035(73)90115-2

Prata, A. J. (1989). Infrared radiative transfer calculations for volcanic ash clouds. *Geophysical Research Letters*, *16*(11), 1293–1296. https://doi.org/10.1029/GL016i011p01293

Prata, A. J., & Grant, I. F. (2001). Retrieval of microphysical and morphological properties of volcanic ash plumes from satellite data: Application to Mt Ruapehu, New Zealand. *Quarterly Journal of the Royal Meteorological Society*, *127*(576), 2153–2179. https://doi.org/10.1002/qj.49712757615

Prata, A. J., & Prata, A. T. (2012). Ejafjallajökull volcanic ash concentrations determined form SEVIRI measurements. *Journal of Geophysical Research*, *117*, D00U23. https://doi.org/10.1029/2011JD016800

Prata, A. J., & Tupper, A. (2009). Aviation hazards from volcanoes: The state of the science. *Natural Hazards*, *51*(2), 239–244. https://doi.org/10.1007/s11069-009-9415-y

Prata, A. J., Woodhouse, M., Huppert, H. E., Prata, A., Thordarson, T., & Carn, S. (2017). Atmospheric processes affecting the separation of volcanic ash and SO2 in volcanic eruptions: Inferences from the May 2011 Grímsvötn eruption. *Atmospheric Chemistry and Physics*, *17*(17), 10,709–10,732. https://doi.org/10.5194/acp-17-10709-2017

Reed, B. E., Peters, D. M., McPheat, R., & Grainger, R. G. (2018). The complex refractive index of volcanic ash aerosol retrieved from spectral mass extinction. *Journal of Geophysical Research: Atmospheres*, *96*, 36–62. https://doi.org/10.1002/2017JD027362

Reed, B. E., Peters, D. M., McPheat, R., Smith, A. J., & Grainger, R. G. (2017). Mass extinction spectra and size distribution measurements of quartz and amorphous silica aerosol at 0.33–19 μm compared to modelled extinction using Mie, CDE, and T-matrix theories. *Journal of Quantitative Spectroscopy and Radiative Transfer*, *199*, 52–65. https://doi.org/10.1016/j.jqsrt.2017.05.011

Rocha-Lima, A., Martins, J. V., Remer, L. A., Krotkov, N. A., Tabacniks, M. H., Ben-Ami, Y., & Artaxo, P. (2014). Optical, microphysical and compositional properties of the Eyjafjallajökull volcanic ash. *Atmospheric Chemistry and Physics*, *14*, 10,649–10,661. https://doi.org/10.5194/acp-14-10649-2014

Rose, W. I., & Durant, A. J. (2009). Fine ash content of explosive eruptions. *Journal of Volcanology and Geothermal Research*, *186*(1–2), 32–39. https://doi.org/10.1016/j.jvolgeores.2009.01.010

Sparks, R. S. J., Wilson, L., & Sigurdsson, H. (1981). The pyroclastic deposits of the 1875 eruption of Askja, Iceland. *Philosophical Transactions of the Royal Society A: Mathematical, Physical and Engineering Sciences*, *A299*(1447), 241–273. https://doi.org/10.1098/rsta.1981.0023

Ventress, L. J., McGarragh, G., Carboni, E., Smith, A. J., & Grainger, R. G. (2016). Retrieval of ash properties from IASI measurements. *Atmospheric Measurement Techniques*, *9*(11), 5407–5422. https://doi.org/10.5194/amt-9-5407-2016

Vogel, A., Diplas, S., Durant, A. J., Azar, A. S., Sunding, M. F., Rose, W. I., Sytchkova, A., et al. (2017). Reference data set of volcanic ash physicochemical and optical properties. *Journal of Geophysical Research: Atmospheres*, *122*, 9485–9514. https://doi.org/10.1002/2016JD026328

Volz, F. E. (1973). Infrared optical-constants of ammonium sulfate, Sahara dust, volcanic pumice, and flyash. *Applied Optics*, *12*(3), 564–568. https://doi.org/10.1364/AO.12.000564

Walter, L. S., & Salisbury, J. W. (1989). Spectral characterization of igneous rocks in the 8- to 12-μm region. *Journal of Geophysical Research*, *94*(B7), 9203–9213. https://doi.org/10.1029/JB094iB07p09203

Watt, S. F. L., Pyle, D. M., Mather, T. A., Martin, R. S., & Matthews, N. E. (2009). Fallout and distribution of volcanic ash over Argentina following the May 2008 explosive eruption of Chaitén, Chile. *Journal of Geophysical Research*, *114*, B04207. https://doi.org/10.1029/2008JB006219

Wen, S., & Rose, W. I. (1994). Retrieval of sizes and total masses of particles in volcanic clouds using AVHRR bands 4 and 5. *Journal of Geophysical Research*, *99*(D3), 5421–5431. https://doi.org/10.1029/93JD03340